Atmospheric forcing of the three-dimensional distribution of dust particles over Australia: A case study

O. Alizadeh Choobari,[1] P. Zawar-Reza,[1] and A. Sturman[1]

Received 8 March 2012; revised 20 April 2012; accepted 24 April 2012; published 5 June 2012.

[1] Knowledge of atmospheric processes responsible for horizontal and vertical distribution of dust particles is important for identifying their transport pathways. The Weather Research and Forecasting with Chemistry (WRF/Chem) model, complemented by observations, was used to simulate and observe the three-dimensional distribution of Australian dust for a severe dust event during 22–23 September 2009. The passage of a cold front modified the boundary layer structure during this event, allowing dust to be lifted and subsequently transported for a significant distance. The model simulated the maximum dust concentrations to be located behind the cold front as a result of strong post-frontal wind speeds. The boundary layer depths were also shown to be significantly deeper behind the cold front where dust particles could be lifted to the top of the boundary layer by turbulent fluxes associated with strong mixing. However, dust was predicted to reach its maximum height ahead of the cold front as a result of lifting in the warm conveyor belt. Both Moderate Resolution Imaging Spectroradiometer (MODIS) data and the WRF/Chem model results for this event highlight two transport pathways of dust: southeastward to the Tasman Sea and northward toward tropical regions of Australia. The vertical distribution of dust from Cloud-Aerosol Lidar with Orthogonal Polarization (CALIOP) satellite data and cross-sectional analysis of the model results indicate that significant amounts of dust aerosols were transported over the Tasman Sea toward New Zealand within the lower atmosphere.

Citation: Alizadeh Choobari, O., P. Zawar-Reza, and A. Sturman (2012), Atmospheric forcing of the three-dimensional distribution of dust particles over Australia: A case study, *J. Geophys. Res.*, *117*, D11206, doi:10.1029/2012JD017748.

1. Introduction

[2] As much of Australia is frequently under the influence of a subtropical high-pressure belt, subsiding air associated with this feature results in an arid or semi-arid climate over much of the interior region of the country. Associated with this arid climate, dust events often occur in the spring, but end in the early summer over northern regions of Australia when the monsoon season starts [*Goudie and Middleton*, 2006]. In contrast, they continue over southern Australia until the end of March [*Shao*, 2008]. Dust storms are often accompanied by strong winds associated with the passage of cold fronts [*McGowan et al.*, 2005] and the subsequent modification of the planetary boundary layer (PBL). Australian dust particles are frequently transported southeastward by prefrontal northwesterly winds [*Knight et al.*, 1995; *McGowan et al.*, 2005] and can, on occasions, reach New Zealand [*Knight et al.*, 1995; *McTainsh et al.*, 2005] where they may degrade air quality. They may also be carried northwestward by southeasterly trade winds [*Shao*, 2008]. In spite of this existing knowledge, further investigation is required to fully understand the atmospheric processes that affect long-range transport of Australian dust and the pathways that it follows.

[3] The spatial distribution of dust over Australia has mostly been studied using such approaches as kinematic trajectory modeling [*McGowan et al.*, 2000], large-scale analysis of surface pressure charts [*McGowan et al.*, 2005; *McTainsh et al.*, 2005] and dispersion and trajectory models [*Knight et al.*, 1995; *McGowan et al.*, 2005]. Although these approaches provide a broad scale view of the movement of dust across the region, they are unable to resolve the impact of boundary layer characteristics and frontogenetically forced vertical motion on the distribution of dust particles. In particular, trajectory approaches can only resolve the advection process and not the smaller scale convection and associated vertical mixing of dust particles present within the boundary layer. Numerical simulation of the 22–23 October 2002 dust event over Australia by *Shao et al.* [2007] identified potential dust sources, as well as the distribution of dust plumes under the action of a frontal system. However, knowledge is still limited of the vertical structure of dust plumes near source regions and during transport, as well as

[1]Center for Atmospheric Research, University of Canterbury, Christchurch, New Zealand.

Corresponding author: O. Alizadeh Choobari, Center for Atmospheric Research, University of Canterbury, Christchurch 8140, New Zealand. (omid.alizadehchoobari@pg.canterbury.ac.nz)

0148-0227/12/2012JD017748

the physical mechanisms responsible for the observed vertical distribution of dust. Indeed, the vertical structure of Australian dust events is poorly understood and is often estimated based on such factors as the height of the subsidence inversion [*McTainsh et al.*, 2005] or qualitative reports based on visual inspection of radar and radiosonde data from airports [*Leys et al.*, 2011]. Given that dust plume height is a key factor for estimating continental dust loss [*Knight et al.*, 1995; *McTainsh et al.*, 2005] and the extent of dust transport [*Huang et al.*, 2006], as well as for assessment of dust radiative forcing [*Chung and Zhang*, 2004], more accurate estimates of the height of Australian dust plumes need to be determined. For example, the distance over which mineral dust is transported is very sensitive to dust layer elevation, as if the dust is able to enter the free atmosphere, it can be transported long distances. Furthermore, previous research suggests that an elevated dust layer has a larger impact on surface cooling than a low-level dust layer [e.g., *Chung and Zhang*, 2004], because heating of the dust layer associated with absorption of shortwave and thermal infrared radiation occurs well above the boundary layer, and is unlikely to be transferred to the surface. Elevated dust aerosols also have longer atmospheric lifetimes than low-level aerosols, so that their radiative impact is more long-lasting.

[4] This paper therefore aims to investigate the three-dimensional distribution of Australian dust during the 22–23 September 2009 dust storm by employing the Weather Research and Forecasting with Chemistry (WRF/Chem) regional model. In particular, this study attempts to identify the role of the major atmospheric mechanisms responsible for dust transport in frontal zones. These processes include those that are responsible for vertical distribution of dust plumes to the top of the boundary layer, horizontal transport of particles by divergent winds from high-pressure systems toward low-pressure regions, and rapid vertical transport of dust particles to the free atmosphere by the warm conveyor belt [*Sinclair et al.*, 2008] where strong ascending motions are present [*Eckhardt et al.*, 2004]. Because of shortcomings in parameterization of the variety of complex physical mechanisms responsible for dust entrainment and its subsequent mixing within the boundary layer in pre- and post-frontal conditions, as well as errors that might be caused by simulation of sub-grid phenomenon, high resolution CALIOP (Cloud-Aerosol Lidar with Orthogonal Polarization) data sets have been used here to provide supporting information on the vertical structure of the dust plumes. The use of CALIOP data, in conjunction with WRF/Chem model results, should help to better understand the three-dimensional distribution of Australian dust.

[5] This study therefore aims to address a number of key questions. First, what are the exit pathways of the dust event and can the WRF/Chem model effectively simulate the spatial distribution of dust during such events? To address this question, model results are analyzed and compared with available satellite data sets, and ground-based measurements in Australia. Second, what atmospheric processes are responsible for the three-dimensional distribution of Australian dust during the passage of a cold front associated with an intense extratropical cyclone? This question cannot be addressed by using observations alone, so that numerical modeling represents a useful tool for extending knowledge of such processes. Finally, what is the vertical and horizontal extent of Australian dust plumes during transport? This question has been addressed using available satellite data in combination with model results.

[6] This paper is organized in the following way. Section 2 describes the model set up and satellite data set. Features of the dust event and its associated synoptic weather conditions are discussed in Section 3, along with the large-scale behavior of the dust plume, while Section 4 presents a comparison of model results with satellite data and ground-based measurements. The impact of frontal systems on boundary layer evolution and the vertical distribution of dust particles are the subject of Section 5. The vertical structure of the dust plumes shown by the CALIOP data set is discussed in Section 6, while a discussion and major conclusions are summarized in Section 7.

2. Numerical Model and Satellite Data

2.1. Numerical Model Description

[7] The WRF/Chem model was set up with 230 × 170 horizontal grid points at 27 km horizontal grid spacing and 27 vertical layers with smaller increments in the lower part of the PBL, for a large domain covering Australia and New Zealand, thereby providing a large-scale synoptic view of weather systems affecting the region. The meteorological initial and boundary conditions come from the National Centers for Environmental Prediction (NCEP) Final Analysis (FNL) re-analysis data at 1° resolution (http://www.nomad3.ncep.noaa.gov/ncep_data), and the boundary conditions were updated every 6 hours, without data assimilation or analysis nudging. The model run was initialized at 0000 UTC on 20 September and continued until 0000 UTC on 26 September, 2009. Biomass burning sometimes occurs in the northern tropical regions of Australia, but its contribution to the aerosols mass is omitted here to focus only on dust transport.

2.1.1. Aerosol and Dust Parameterization Schemes

[8] The aerosol parameterization is based on the Model for Simulating Aerosol Interactions and Chemistry (MOSAIC) [*Zaveri et al.*, 2008] with 8 sectional bins for aerosols less than 10 μm (6 bins are for particles less than 2.5 μm ($PM_{2.5}$) and 2 bins for particles between 2.5 and 10 μm). Dry deposition includes turbulent and molecular diffusion, as well as gravitational settling which was configured in the simulation based on the approach of *Binkowski and Shankar* [1995]. Wet deposition via in-cloud and below-cloud scavenging was also included in the simulation. In the in-cloud process, dust particles form condensation nuclei that are captured by water droplets that grow on them, while in the below-cloud process, raindrops scavenge dust particles as they fall.

[9] The dust emission scheme is based on the dust transport (DUSTRAN) module developed by *Shaw et al.* [2008] which has been modified to adjust it to the 24-category USGS land-use classes of WRF, which are different from the 59 land-use categories of the Olson database used in *Shaw et al.* [2008]. Vertical dust flux from the surface was approximated by *Shaw et al.* [2008], as follows:

$$F = \alpha C u_*^4 \left(1 - \frac{f_w u_{*t}}{u_*}\right) \quad for \quad u_* \geq u_{*t} \tag{1}$$

Table 1. Fractions ($\beta_{k,j}$) of the Soil Texture Categories in Each Zobler Soil Class[a]

		$\beta_{k,j}$			
j	Zobler Soil Classes	Clay (k = 1)	Small Silt (k = 2)	Large Silt (k = 3)	Sand (k = 4)
1	Coarse	0.12	0.04	0.04	0.80
2	Medium	0.34	0.28	0.28	0.10
3	Fine	0.45	0.15	0.15	0.25
4	Coarse-medium	0.12	0.09	0.09	0.70
5	Coarse-fine	0.40	0.05	0.05	0.50
6	Medium-fine	0.34	0.18	0.18	0.30
7	Coarse-medium-fine	0.22	0.09	0.09	0.60

[a]After *Shaw et al.* [2008].

where α is the vegetation mask that ranges from zero to 1 and depends on vegetation cover, C (g cm^{-6} s^{-3}) = 1.0×10^{-14} is a dimensional empirical constant, u_{*t} (cm s^{-1}) is the threshold friction velocity below which there is no dust emission, considered here to be 20 cm s^{-1}, u_* (cm s^{-1}) is the friction velocity relating to the downward transfer of momentum flux to the surface ($u_* = \sqrt{\tau/\rho}$, where τ is shear stress at the surface and ρ is air density), and f_w is the soil wetness factor, which is estimated based on the approximation of *Fecan et al.* [1998]:

$$f_w = \begin{cases} \sqrt{1 + A(w - w')^b} & w > w' \\ 1 & w \le w' \end{cases} \quad (2)$$

where ω (%) is the gravimetric soil moisture or ground wetness $\left(\frac{mass\ of\ water}{mass\ of\ soil} \times 100\right)$ and obtained by converting model soil moisture ($\frac{m^3}{m^3}$) assuming a constant soil density of 2.6 g cm^{-3}:

$$w = \frac{soil\ moisture}{2.6} \times 100 \quad (3)$$

The coefficients A = 1.21 (indicating soil structure) and b = 0.68 (indicating moisture tension) were found by *Fecan et al.* [1998] on the basis of empirical data and ω' denotes the maximum amount of water that can be absorbed by the soil and is a function of soil clay content:

$$w' = 0.0014\beta_1^2 + 0.17\beta_1 \quad (4)$$

where β_1 is fraction of clay content in the soil as a percentage for 7 different Zobler soil classes ($\beta_1 = \beta_{1,j} \times 100$, where j = 1, . , 7 denotes the 7 Zobler classes; see Table 1). Since there are 16 soil classes in the WRF model which are different from the 7 Zobler soil categories used in *Shaw et al.* [2008], the WRF soil classes were mapped to Zobler soil categories as shown in Table 2. Note that the DUSTRAN module in the WRF/Chem model skips dust computations for WRF soil classes greater than 13, including organic material, water, bedrock and other types, such as land-ice. Based on equation 4 and Table 1, ω' increases with the soil clay content, indicating that clay particles increase the adsorption capacity of soil. Equation 2 implies that when the soil moisture (ω) is smaller than the maximum amount of water that can be trapped by the soil (ω'), the wetness factor does not influence the erosion threshold, meaning that ω' corresponds to the minimum amount of soil moisture from which the threshold friction velocity increases [*Shaw et al.*, 2008].

[10] The initial background dust concentrations at the start of the simulation are considered to be zero by the model and there is no lateral inflow of dust from outside of the domain, as the model assumes that all dust comes from the interior of the simulation domain, but dust can be freely advected out of the domain when it reaches the lateral boundaries. These assumptions mean that the model neglects the contribution of external sources and background aerosols. The model was initialized in the simulation at 0000 UTC on 20 September, which is at least two days before the cold front started to influence dust transport from local dust sources, while dust from outside the region is not considered of concern as Australia is located far from other source regions of dust, and therefore, unlikely to be significantly affected by them.

Table 2. WRF Soil Classes Corresponding to the Seven Zobler Soil Categories

j	WRF Soil Classes	j	Zobler Soil Classes
1	Sand	1	Coarse
2	Loamy sand	1	Coarse
4	Silt loam	2	Medium
5	Silt	2	Medium
6	Loam	2	Medium
8	Silty clay loam	2	Medium
11	Silty clay	2	Medium
12	Clay	3	Fine
3	Sandy loam	4	Coarse-medium
10	Sandy clay	5	Coarse-fine
9	Clay loam	6	Medium-fine
7	Sandy clay loam	7	Coarse-medium-fine

Table 3. WRF/Chem Model Configuration[a]

Physical Process	WRF/Chem Option
Microphysics	Lin [*Lin et al.*, 1983]
Short-wave radiation	Goddard [*Wild et al.*, 2000]
Long-wave radiation	RRTM [*Wild et al.*, 2000]
Surface layer	Monin-Obukhov [*Obukhov*, 1971]
Land-surface model	NOAH [*Chen and Dudhia*, 2001; *Ek et al.*, 2003]
Boundary layer scheme	YSU [*Hong et al.*, 2006; *Hong*, 2010]
Cumulus parameterization	Grell 3D [*Grell*, 1993]
Aerosol module	MOSAIC 8-bin [*Zaveri et al.*, 2008]
Dust scheme	DUSTRAN [*Shaw et al.*, 2008]

[a]Adapted from *Chapman et al.* [2009].

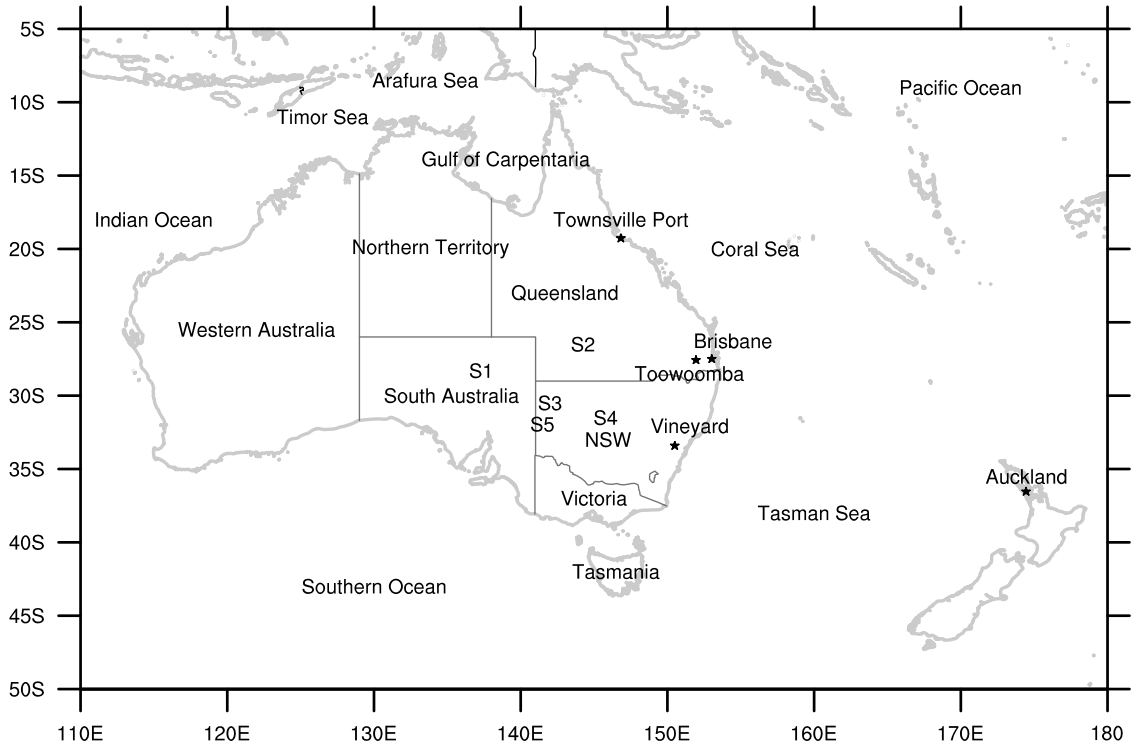

Figure 1. Position of Australian states and surrounding oceans and seas, the location of the main potential sources of dust: Lake Eyre Basin (S1), the Channel Country (S2), grazing lands in the northwest of New South Wales (NSW, S3), mining areas near Cobar (S4) and Broken Hill (S5), and places mentioned in the text.

2.1.2. Boundary Layer Parameterization Scheme

[11] The main physics options used in the WRF/Chem simulation are listed in Table 3. The PBL scheme is particularly noteworthy as the vertical dust flux in equation 1 is proportional to the shear stress via the friction velocity, which itself is strongly related to the turbulent fluxes within the boundary layer. Furthermore, boundary layer structure plays a critical role in both the vertical distribution and amount of dry deposition of dust, as well as transport of dust away from the surface to the top of the boundary layer.

[12] The PBL parameterization implemented in the WRF is based on the Yonsei University (YSU) scheme [*Hong et al.*, 2006; *Hong*, 2010]. The YSU scheme is a nonlocal closure model, which incorporates the contribution of large-scale eddies to the total flux. The nonlocal scheme includes a counter-gradient flux term, enabling realistic simulation of a well-mixed layer [*Hong et al.*, 2006; *Hong*, 2010]. The boundary layer top is defined as the height at which a critical bulk Richardson number ($Ri_{b,cr}$) reaches a constant value of 0.25 over land, but over ocean it is derived from [*Hong*, 2010]:

$$Ri_{b,cr} = 0.16\left(10^{-7}Ro\right)^{-0.18} \tag{5}$$

where Rossby number (Ro) is defined as [*Hong*, 2010]:

$$Ro = \frac{U_{10}}{f_0 z_0} \tag{6}$$

where U_{10} is the wind speed at 10 meters, f_0 the Coriolis parameter, and z_0 the surface roughness length. This method takes into account both buoyancy and mechanical mixing, thereby representing a realistic atmospheric boundary layer.

2.2. Satellite Data Description

[13] Moderate Resolution Imaging Spectroradiometer (MODIS) instruments were launched on board NASA's Terra and Aqua satellites in 1999 and 2002, respectively, providing continuous multichannel measurements over ocean and land surfaces, allowing retrieval of aerosol optical properties. The retrieved aerosol optical depth (AOD) values are estimated to be reasonably accurate over the oceans, while accuracy decreases over land surfaces, and aerosol retrievals are limited over highly reflective land surfaces [*Remer et al.*, 2005].

[14] A polarization-sensitive backscatter lidar known as CALIOP was launched on board NASA's Cloud-Aerosol Lidar and Infrared Pathfinder Satellite Observations (CALIPSO) satellite on 28 April 2006 [*Winker et al.*, 2007]. Since then, CALIOP has provided nearly continuous vertical profiles of aerosols and clouds globally, offering a unique opportunity to study vertical structure and transport of dust, as well as its optical properties. Nevertheless, CALIOP is unable to detect accurate aerosol profiles under thick aerosol and cloudy conditions, and when the quantity of aerosols is below its detection threshold.

[15] CALIOP operates at 532 nm and 1064 nm. The Level 1B and Level 2 CALIOP data sets have been used in this study. The Level 1B (version 3.01) provides vertical profiles of the total attenuated backscatter coefficient at 532 nm (with horizontal and vertical resolutions of 333 m and 30 m,

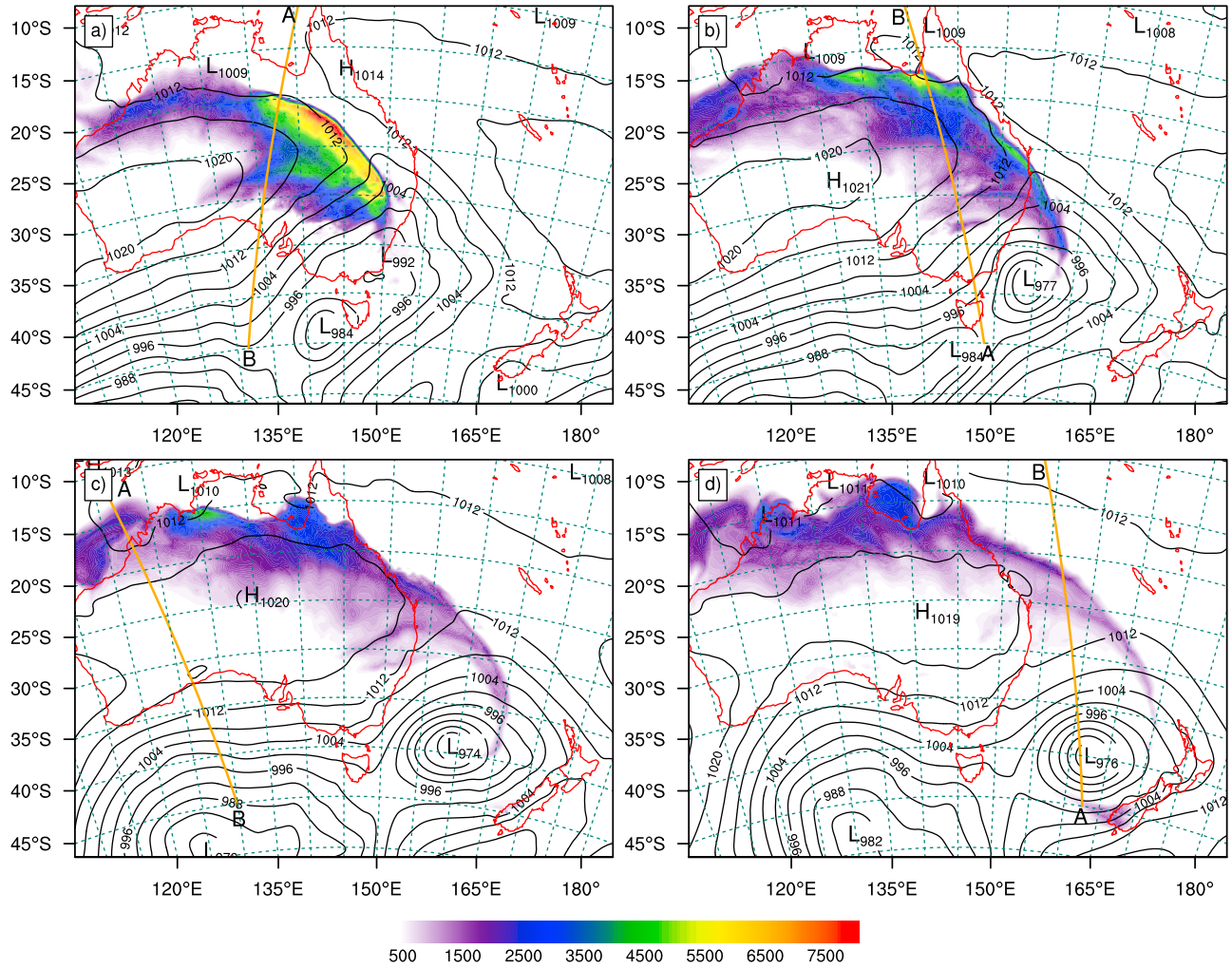

Figure 2. Simulated mean sea level pressure (contour interval of 4 hPa) and surface PM_{10} concentrations ($\mu g\ m^{-3}$, as shown in scale) over Australia at (a) 1600 UTC on 22 September, (b) 0400 UTC on 23 September, (c) 1700 UTC on 23 September, and (d) 0300 UTC on 24 September 2009. The orange lines labeled A and B show the CALIPSO orbit paths and their vertical cross-sections are plotted in Figures 12 and 13.

respectively) and 1064 nm (with horizontal and vertical resolutions of 333 m and 60 m, respectively) and the attenuated depolarization ratio at 532 nm. The depolarization ratio is the ratio of perpendicular to parallel components of received lidar signals at 532 nm, and is large for dust particles due to their non-sphericity [*Huang et al.*, 2009], so that they can be easily distinguished from other aerosols. Aerosol extinction coefficient profiles were derived from the Lidar Level 2 CALIOP data (with horizontal and vertical resolutions of 5 km and 300 m, respectively) during CALIOP flights over the Australian continent. Cloud-aerosol discrimination (CAD), an indicator used to discriminate between cloud (positive CAD) and aerosols (negative CAD), is used to exclude extinction caused by clouds.

3. The 22–23 September Dust Episode

3.1. Dust Event Features

[16] The severe dust event during 22–23 September 2009 over Australia was associated with a cold front that produced limited precipitation and strong wind speeds. Prior to this intensive dust event, there was a severe drought over large parts of Australia for several years [*Zhao and Running*, 2010], combined with a record of very high maximum temperatures in 2009 [*Trewin and Vermont*, 2010], that contributed to an extreme soil moisture deficit and reduced vegetation cover. Correlation between Australian drought periods and the El Niño Southern Oscillation (ENSO) phenomenon has been found from records in the past [*McTainsh et al.*, 2005]. As a result of such extreme meteorology and drought conditions, the dust storm was one of the severest dust events since 1940, with the maximum hourly averaged PM_{10} concentrations exceeding 15,000 $\mu g\ m^{-3}$ at Bathurst (15,388 $\mu g\ m^{-3}$) and Bringelly (15,366 $\mu g\ m^{-3}$) air quality monitoring sites in New South Wales [*Leys et al.*, 2011]. The network of ground-based measurement sites captured southeastward transport of Australian dust reaching Auckland, which is ~3600 km from the Lake Eyre Basin, Australia's most active dust source, producing PM_{10} concentrations reaching ~350 $\mu g\ m^{-3}$. These ground-based measurements indicate that dust transport from Brisbane on the east coast of Australia to the North Island of New Zealand (a ~2270 km

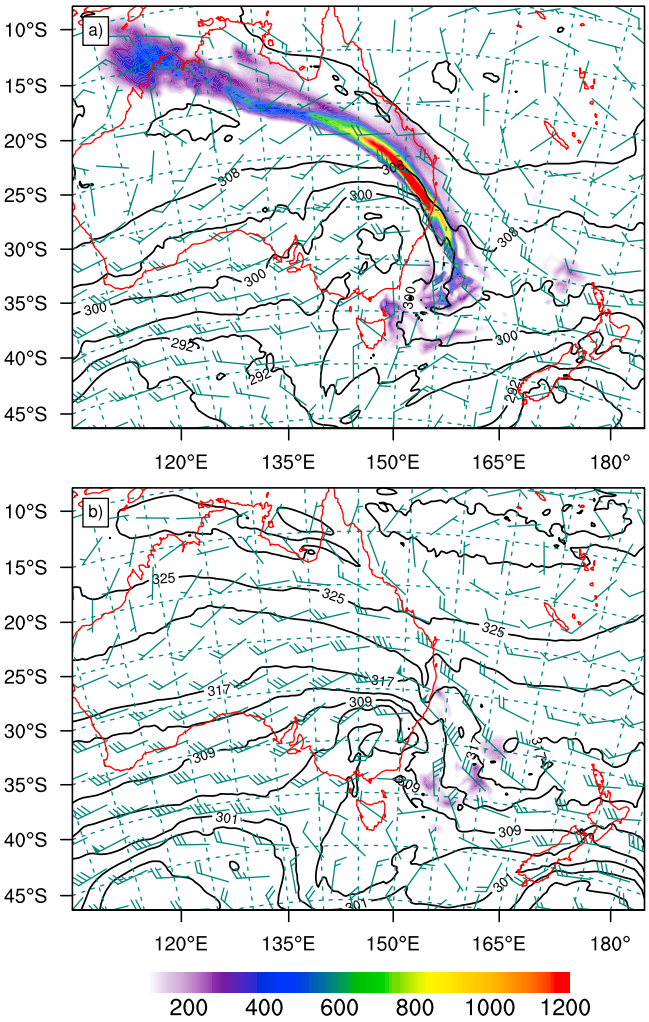

Figure 3. Simulated potential temperatures (contour interval of 4 K), horizontal wind speed (m s^{-1}) and PM_{10} concentrations (μg m^{-3}, as shown in scale) over Australia at 0000 UTC on 23 September at (a) 700 hPa and (b) 500 hPa. In the wind vector scale, one full barb represents 10 m s^{-1}, with a solid triangle representing 50 m s^{-1}.

distance) took approximately 1 day and 9 hours. The major dust emission sources in the region for this event have been determined to be Lake Eyre Basin (S1) in central southern Australia, the Channel Country (S2) in western Queensland, grazing land in northwestern New South Wales (S3), and mining areas near Cobar (S4) and Broken Hill (S5) [*Leys et al.*, 2011]. Figure 1 shows the location of these major dust sources, as well as the Australian territories and surrounding seas mentioned in the text.

3.2. Synoptic Conditions During the Dust Storm and Large-Scale Behavior of the Dust Plume

[17] A strong midlatitude cyclone (the minimum pressure that the cyclone achieved was simulated to be 974 hPa at 1700 UTC on 23 September 2009, see Figure 2c) crossed the Southern Ocean to the southeast of Australia (Figure 2a), and gradually intensifying over the next 24 hours as it moved further east (Figures 2b and 2c). By 0300 UTC on 24 September, the cyclone moved over the eastern Tasman Sea, while Australia was completely dominated by a high-pressure system (Figure 2d).

[18] Figure 2a suggests that dust particles were initially entrained by strong cold post-frontal southwesterly winds associated with the deep cyclonic system. The model simulated significant dust concentrations as a result of strong near-surface wind speeds that can be identified by tightly packed isobars. Dust particles were initially transported to northeastern Australia by these post-frontal southwesterly winds (Figures 2b and 2c), and to the Tasman Sea by pre-frontal northwesterly winds (Figures 2b, 2c and 2d). Model results also highlight transport of dust that was oriented from eastern central Australia to the northern tropical regions, and later to northwestern Australia under the influence of the anticyclonic circulation, with dust finally being advected to the Indian Ocean. By 0300 UTC on 24 September, part of the dust plume was predicted to have moved southeastward to the eastern Tasman Sea (Figure 2d), creating an arc shape to the dust clouds.

[19] The long distance transport to the southeast appears to be due to the dominance of westerlies at higher altitudes both over the midlatitudes and tropical regions (see Figure 3b). Also, strong fronts are typically associated with strong frontal jets that run parallel to the temperature gradient, strengthening northwesterly flows. This long-range southeastward transport is evident in the high PM_{10} concentrations observed at Auckland, New Zealand, as discussed earlier. The small amounts of dust predicted to occur only over the Tasman Sea at the 500 hPa level (Figure 3b), confirm that in the mid-troposphere, dust was only transported southeastward. Furthermore, the simulated PM_{10} concentrations at 700 hPa and 500 hPa (Figure 3) suggests that some of the dust particles over the Tasman Sea were transported in the opposite direction to the movement of the cyclonic weather system, reflecting the cyclonic turning within the warm conveyor belt. This rearward motion is also reflected in the potential temperature contours around the cyclonic circulation in Figure 3. It seems that dust was located within the warm conveyor belt and hence the transport pathway appears to be determined by the rising motion that occurs within this feature. As the dust seems to have been initially lifted from the surface into the atmosphere behind the cold front by strong winds, it appears that dust was transported through the frontal zone before being advected by the warm conveyor belt.

4. Comparison With Satellite and Ground-Based Measurements

4.1. Satellite Data

[20] Aerosol optical depth, attenuation of solar radiation by atmospheric aerosols, at 0.55 μm over both ocean and land at around 0100 UTC on 23 September and 0000 UTC on 24 September 2009 were obtained from the MODIS data set and simulated by the WRF/Chem model (Figure 4). Figure 5 also reveals eight-day (22–29 September 2009) AOD values at 0.55 μm retrieved from the MODIS data set. White regions in the MODIS image denote areas with no satellite measurements, either because of high surface albedo over bright surfaces or thick cloud cover. As the single-view sensors of the MODIS instrumentation are not able to differentiate between the visible solar radiation reflected by

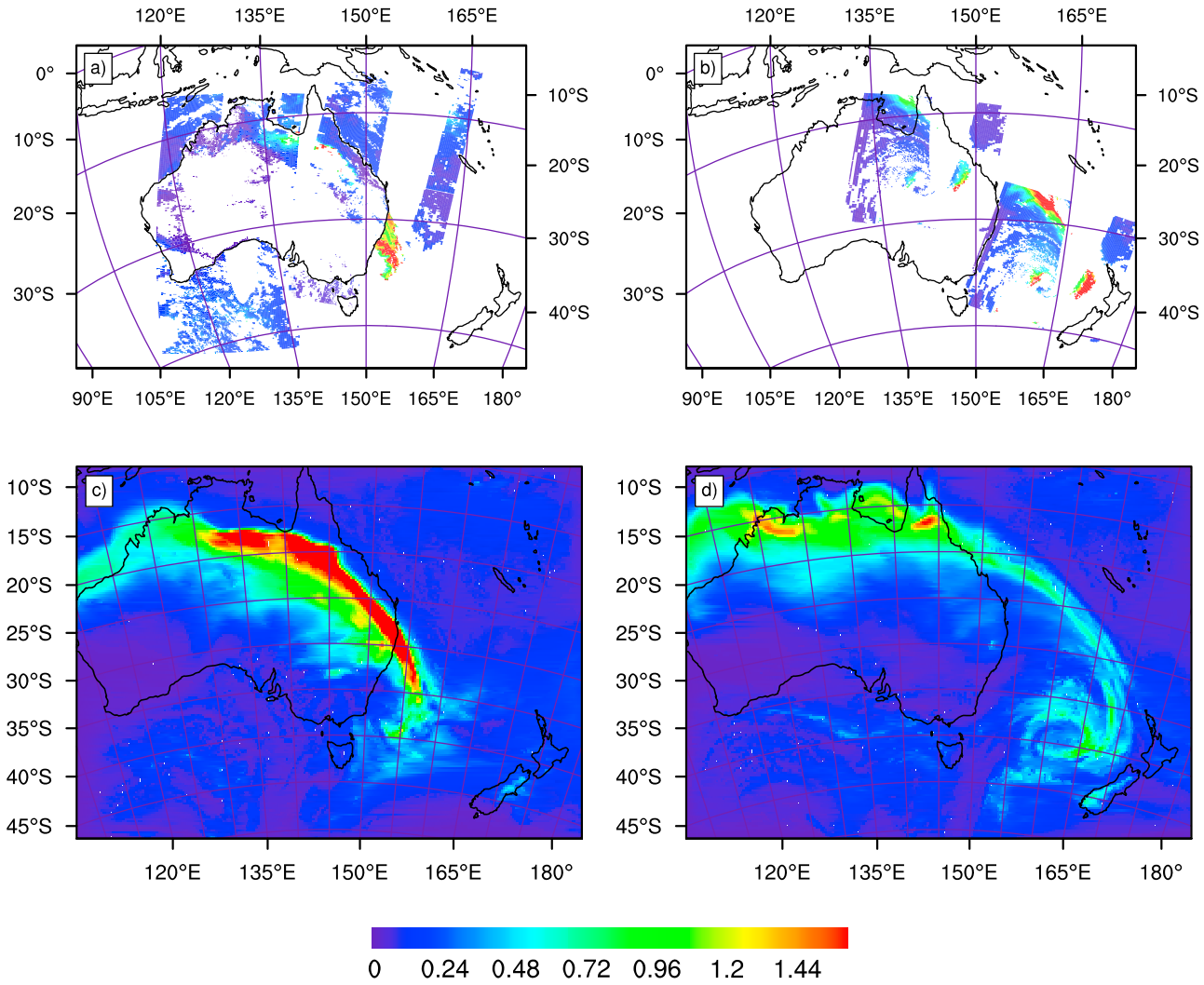

Figure 4. Comparison of aerosol optical depth (AOD) at 0.55 μm (a, b) derived from MODIS on board the Terra satellite and (c, d) simulated by the WRF/Chem model at around 0100 UTC on 23 September (Figures 4a and 4c) and 0000 UTC on 24 September 2009 (Figures 4b and 4d).

atmospheric aerosols from that reflected by the bright ground surfaces (note that most of the Australian land surface is covered by deserts), comparison of the model results and the MODIS data set is not reliable over land surfaces and only really possible over ocean. It should be noted that biomass burning is visible in satellite data (not shown) in the Queensland region (around 25°S and 147°E) on 24 September. These fires make it difficult to distinguish between the retrieved AOD from MODIS (Figures 4b and 5) originating from mineral dust aerosols and smoke from biomass burning.

[21] Model simulations indicate that high AOD values extended from the Tasman Sea, offshore of the Australian east coast, to northeastern and northern Australia on 23 September (Figure 4c), showing some similarity to the MODIS measurements over the Tasman Sea (Figure 4a). Therefore, the modeled dust plume is approximately in the right location, although the model simulation overestimated aerosol concentrations extending from the northwest coast of Australia to the Indian Ocean (where the MODIS data set shows comparatively small amounts). As discussed earlier, the anticyclonic circulation (shown in Figure 2) was responsible for transport of dust across northern Australia toward the Indian Ocean. High AOD values can be observed over the eastern part of the Tasman Sea, close to New Zealand at 0400 UTC on 24 September (Figure 4b). This pattern is quite well represented by the WRF/Chem model in Figure 4d, but with lower values. Overall, both simulation results and MODIS data indicate southeastward transport of dust to the Tasman Sea by the eastward propagating frontal system and to northern Australia by post-frontal southerly winds.

[22] The eight-day AOD values obtained from MODIS indicate high AOD values off the southeast coast of Australia over the Tasman Sea (Figure 5), quite similar to the simulated AOD at 0100 UTC on 23 September (Figure 4c). It is highly likely that the aerosol plume would have extended over the Australian land area as well, because the aerosols mainly originated from the Australian deserts, but the MODIS instrumentation was not able to detect it adequately over the land area (for the reasons mentioned earlier). MODIS data also reveal moderate to high AOD values extending from the Coral Sea off the northeast coast of

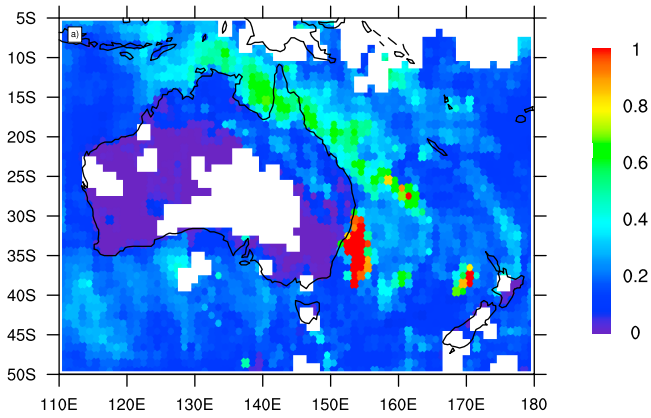

Figure 5. Eight-day aerosol optical depth (AOD) at 0.55 μm from 22–29 September 2009 retrieved from the MODIS data set.

Australia toward the Gulf of the Carpentaria and the Arafura Sea to the north of the country, as well as to the Timor Sea to the northwest. Notice that the coastline of north and northeastern Australia is coincident with a sharp gradient in aerosol concentrations in Figure 5, except for northern Queensland, which strongly supports the argument that MODIS instrumentation was not able to accurately detect the aerosol concentrations over land, due to variations in surface albedo. As the source of dust is located on the Australian continent, it is safe to conclude that in reality significantly higher AOD values extended over northeastern Australian land toward the north and northwest, as shown in the model results in Figure 4c. The concentrations of aerosols simulated by the model and observed in the eight-day MODIS data set over the Southern Ocean, off Australia's south coast, are likely caused by sea salt due to increased wind speed associated with the low-pressure system moving across the Southern Ocean.

4.2. In Situ Measurements

[23] Ground-based hourly averaged PM_{10} measurements obtained from air quality stations along the east coast of Australia (sites shown in Figure 1) and their comparison with simulated values are displayed in Figure 6. It should be noted that model values are representative of 27 $\times$ 27 km grid cells, while observations are point measurements. A comparison of the maximum simulated and observed PM_{10} concentrations and the time of their occurrence for these stations are shown in Table 4. The observed and simulated peak PM_{10} concentrations at Toowoomba occurred about 2 hours before the peak values at Brisbane to the east, indicating the eastward propagation of the dust plume. Furthermore, observed peak PM_{10} values decreased from south (Vineyard) to north (Townsville Port), due to the greater distance from major dust source regions as one moves to the north [*Leys et al.*, 2011].

[24] For Brisbane and Toowoomba, the simulated PM_{10} concentrations followed the observations very well, and there is good agreement between the observed and simulated peak values, although the peaks were simulated 2 hours prior to the measurements and are less than observed values. Before and after the time of peak values when near-surface wind speeds were generally weaker, the simulated PM_{10} concentrations exceeded those observed. This bias arises because the threshold friction velocity is considered to be independent of particle size, having the constant value of 20 cm s^{-1}, causing the tendency to overestimate dust emission at weaker wind speeds, as the stronger cohesive bonds between fine silt and clay particles are not considered. The similar pattern of PM_{10} concentrations observed and simulated at Brisbane and Toowoomba indicates that dust was being transported through the region rather than being entrained within it, otherwise local dust emission would have modified dust plume characteristics between sites, resulting in large variations in dust concentration over short distances [*Leys et al.*, 2011].

[25] For Townsville Port, the model correctly simulated the time of dust arrival and temporal evolution, but overpredicted the PM_{10} concentrations by a factor of 2. PM_{10} concentrations stayed high for a long time compared to other stations, suggesting that the site is located downwind of a source that continued to supply dust for an extended period of time [*Leys et al.*, 2011]. For Vineyard, the observed peak value exceeded the simulated peak value substantially. The underestimation of PM_{10} concentrations can be related to the underestimation of dust emission over source regions in New South Wales (S3, S4 and S5, shown in Figure 1). These areas could have acted as potential sources of dust, as prior to the dust event, there was a severe drought over the region.

5. Atmospheric Forcing of the Distribution of the Dust Plume

5.1. Boundary Layer Evolution During the Episode

[26] Figure 7a clearly predicts considerable development of deep boundary layer depths behind the cold front, driven by conditional instability close to the surface due to strong cold advection. Cold southwesterly air crossing the Southern Ocean onto the Australian land mass would have experienced significant heating as it moved across the surface that was still warm from the previous day, leading to deep boundary layer development and subsequent vertical mixing. Bearing in mind that Figure 7a shows the situation at 0400 Eastern Standard Time (UTC + 10), synoptic-scale forcing would have been largely responsible for the evolution of the boundary layer rather than daytime heating. Similar development of a deep boundary layer behind a cold front caused by strong cold advection over the Atlantic Ocean was also evident in simulations performed by *Sinclair et al.* [2010]. In contrast, warm advection in the warm sector of the cyclone (to the northeast of the low-pressure center) was associated with negative buoyancy, which reduced buoyancy-driven turbulent mixing, preventing the boundary layer from becoming well-mixed. As a result, there are notably shallower boundary layer depths in this area due to a more stable boundary layer. It should be noted that even during warm air advection, shear-driven turbulence can cause the boundary layer structure to evolve and reach moderate depths.

[27] Figure 8a depicts a vertical cross-section perpendicular to the cold front along the line A to B in Figure 7a, showing potential temperature contours, boundary layer depth, PM_{10} concentration and vertical velocity. The boundary layer development behind the cold front can be related to enhanced

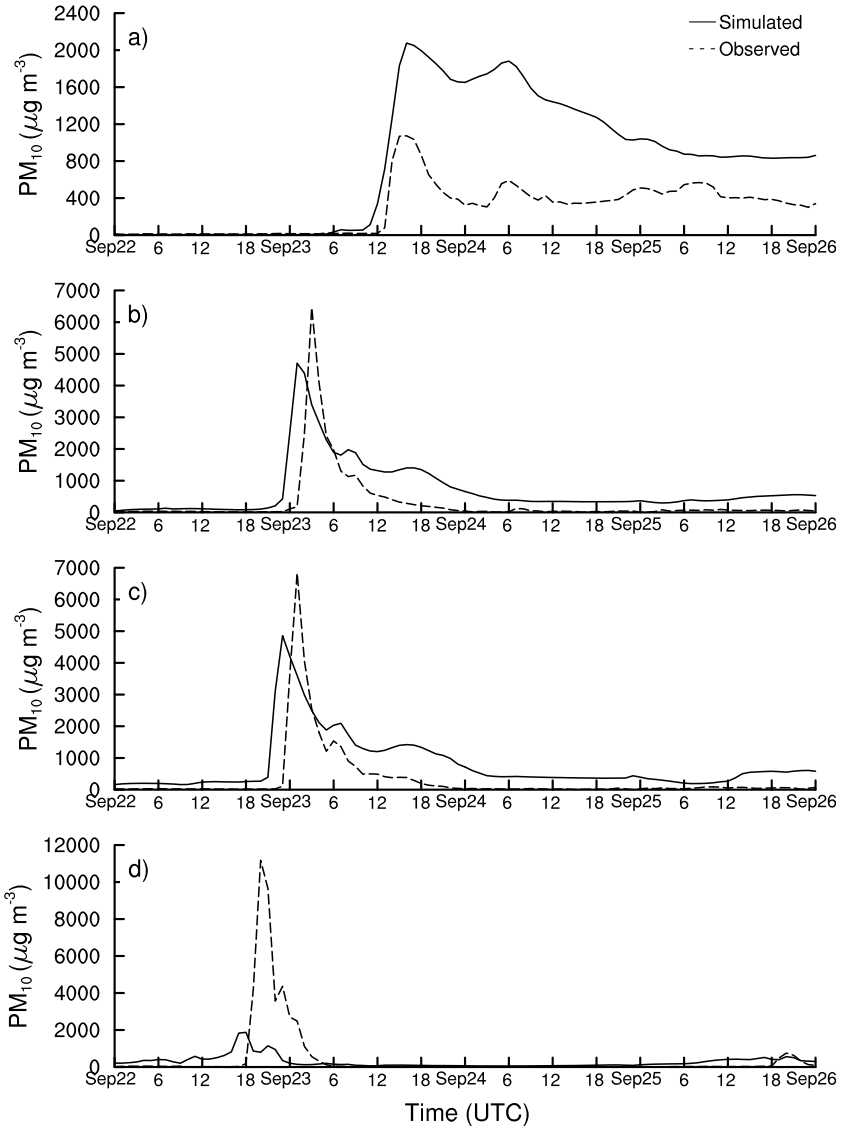

Figure 6. Hourly averaged PM_{10} concentrations ($\mu g\ m^{-3}$) measured (dashed line) and simulated (solid line) at four Australian air quality monitoring sites: (a) Townsville Port (19.25°S, 146.83°E) in central Queensland, (b) Brisbane CBD (27.48°S, 153.03°E), (c) Toowoomba (27.55°S, 151.95°E), both in south Queensland, and (d) Vineyard (33.39°S, 150.50°E) in New South Wales, Australia during 22–26 September 2009. Note the different Y axis scales in all panels. Locations of the air quality monitoring sites are shown in Figure 1.

vertical mixing, which increases near-surface wind speeds, leading to an increase of wind erosion and thus dust entrainment. Turbulent eddies associated with this well-mixed boundary layer are expected to have carried dust particles to the top of the boundary layer, and subsequent entrainment into the free atmosphere (as shown in Figure 8a). The reason that dust particles are predicted to have escaped from the boundary layer behind the cold front is partly due to the fact that the YSU

Table 4. Maximum PM_{10} Concentrations ($\mu g\ m^{-3}$) and the Time of Their Occurrence Observed and Simulated by the WRF/Chem Model During the 22–23 September 2009 Dust Event

		PM_{10} ($\mu g\ m^{-3}$)		Time (UTC)	
Station	Location	Observed	Simulated	Observed	Simulated
Townsville Port	19.25°S, 146.83°E	1073	2076	23 Sep 1600	23 Sep 1600
Brisbane CBD	27.48°S, 153.03°E	6459	4703	23 Sep 0300	23 Sep 0100
Toowoomba	27.55°S, 151.95°E	6834	4858	23 Sep 0100	22 Sep 2300
Vineyard	33.39°S, 150.50°E	11174	1876	22 Sep 2000	22 Sep 1800

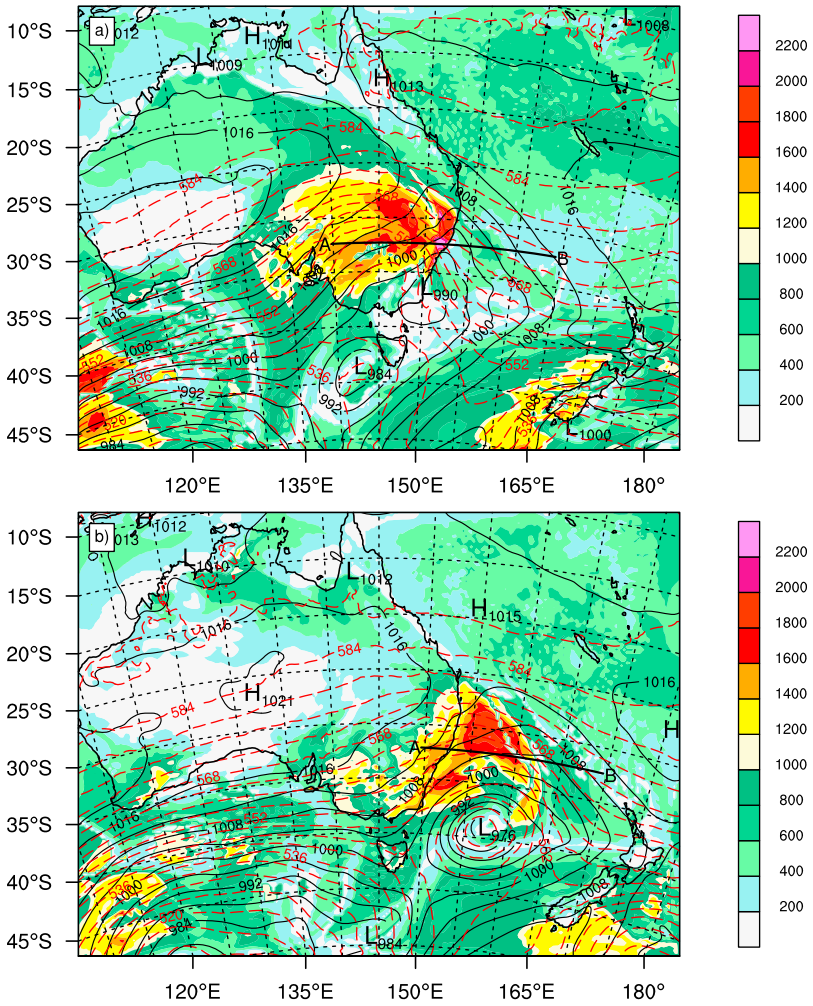

Figure 7. PBL depth (m, as shown in scale), mean sea level pressure (solid black contours with an interval of 4 hPa) and geopotential height contours at 500 hPa (dashed red contours with an interval of 4 dm) simulated by the WRF/Chem model at (a) 1800 UTC on 22 September and (b) 1200 UTC on 23 September 2009. The bold black lines from A to B mark the vertical cross-sections plotted in Figure 8.

PBL scheme defines the boundary layer top as the level at which still minimum turbulent mixing occurs [*Hong*, 2010]. Despite weak, or even a lack of, upward vertical motion behind the cold front (Figure 8a), the predicted vertical transport of particles through the depth of the boundary layer and to the lower layers of the free atmosphere indicates the importance of turbulent mixing for the vertical distribution of dust plumes. Note that the potential temperature contours slope backwards behind the cold front, demonstrating rearward tilting of the cold front with height.

[28] There is a sharp decrease in boundary layer depth from behind to ahead of the cold front (Figures 7a and 8a). However, ahead of the surface cold front, dust plumes are predicted to extend to a greater depth, reaching to approximately 8 km as a result of ascending motion in the warm conveyor belt (Figure 8a), demonstrating the contribution of dust to background tropospheric aerosols over the Australian region. The ascending motion in the warm conveyor belt is evident in the strong positive vertical velocities at the leading edge of the cold front, demonstrating frontogenetically induced vertical motions. The positive vertical velocities in the warm sector are consistent with the quasigeostrophic omega equation which indicates that warm advection is accompanied by rising motion when temperature and horizontal wind fields are sinusoidal [*Bluestein*, 1992].

[29] Further west of the cold front, over the Australian continent, descending motion associated with the establishment of the anticyclonic circulation appears to be responsible for strong capping of the vertical extent of dust (Figure 8a). Consequently, the dust plumes are shown to be restricted to the lower atmosphere (below ~1.2 km), which can contribute to the increase of dry deposition. Furthermore, large-scale descending motion over the region associated with anticyclonic circulation contributes to divergent wind flows toward surrounding low-pressure regions. This motion is a key mechanism to advect particles horizontally to the warm conveyor belt region where there is a greater potential for the particles to be transported vertically to the free atmosphere [*Sinclair et al.*, 2008]. This suggests that warm conveyor belt ascent is the main process acting to transport particles to the free atmosphere [*Kowol-Santen et al.*, 2001; *Sinclair et al.*, 2008], so that they can be

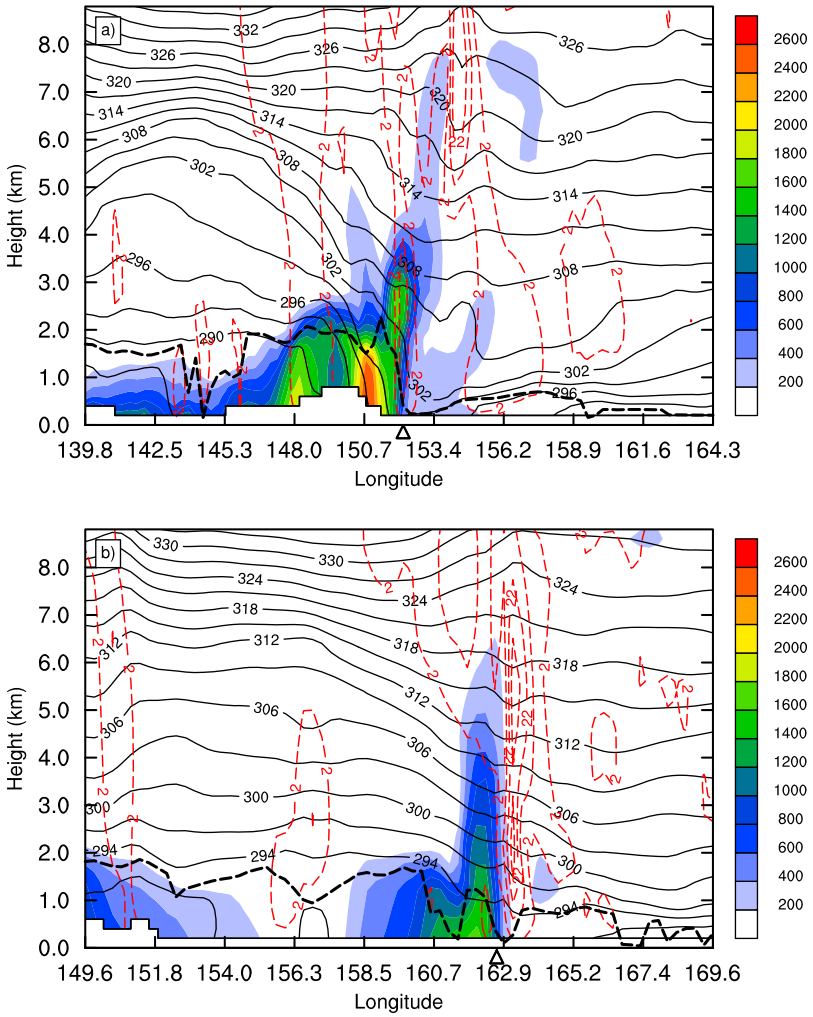

Figure 8. Simulation of vertical cross-sections of potential temperature (solid lines with a contour interval of 3 K), PM_{10} concentrations (μg m^{-3}, as shown in scale), vertical velocity (dashed red lines with contour interval of 10 cm s^{-1}) and PBL depth (dashed black line, km) perpendicular to the cold front along the line from A to B shown in Figure 7 at (a) 1800 UTC on 22 September and (b) 1200 UTC on 23 September 2009. The approximate location of the cold front is shown by the arrow on the X axis. For clarity, only positive vertical velocities greater than 2 cm s^{-1} have been plotted, and it should be noted that Figures 8a and 8b cover different horizontal distances.

subsequently transported over long distances by strong upper-level wind flows. Turbulent mixing behind the cold front is also an important mechanism in the vertical transport of particles to the free atmosphere as it pushes particles to the altitudes where divergent motions from anticyclonic toward cyclonic circulation are stronger [*Sinclair et al.*, 2008]. Even with the strong ascending motions ahead of the cold front, PM_{10} concentrations remained high near the surface, demonstrating the supply of dust particles through horizontal motions. This is also partly due to the fact that dust is mainly composed of coarse particles and its vertical transport is restricted by gravitational settling.

[30] The predicted impact of the frontal system on the nighttime evolution of the marine boundary layer at 1200 UTC on 23 September 2009 is shown in Figure 7b. The boundary layer is deep behind the cold front extending from the central Tasman Sea to the coastal regions of southeastern Australia. Relatively shallow boundary layer depths can be seen in the warm sector ahead of the cold front due to warm advection over colder surfaces. However, the lowest boundary layer depths are located over central and western Australia where they are dominated by a high-pressure system with a central pressure of 1021 hPa.

[31] A vertical cross-section perpendicular to the cold front, along the line AB in Figure 7b, shows that the plume of dust was advected up to around 6 km both behind and along the leading edge of the cold front (Figure 8b). The elevated PM_{10} concentrations are located to the west of the strong ascent in Figure 8b, while Figure 8a shows the high PM_{10} concentrations to be co-located with the strong frontal ascent. One possible cause for the difference is that the strong ascent would have been associated with high concentrations of dust when the frontal zone was moving over the source regions of dust and nearby areas, but as it moved

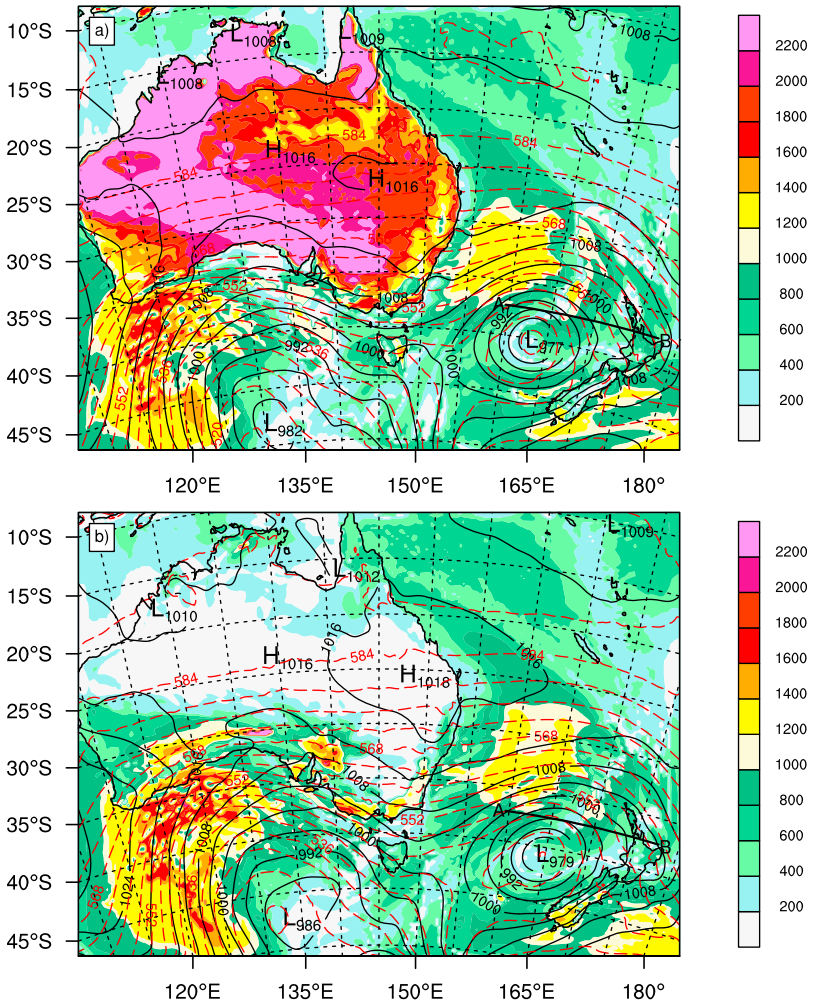

Figure 9. Similar to Figure 7 but at (a) 0600 UTC on 24 September and (b) 1200 UTC on 24 September 2009. The bold black lines from A to B mark the vertical cross-sections plotted in Figure 10.

away from the source regions to the Tasman Sea the rising air would have been increasingly dust-free, leaving the residual dust in the air lagging behind the front. Note that the PM_{10} concentrations are significantly reduced from a maximum concentration of ~2600 μg m^{-3} in Figure 8a to ~1600 μg m^{-3} in Figure 8b, demonstrating substantial dust loss during the transport from eastern Australia to the Tasman Sea.

[32] Surface and mid-troposphere analysis of the low-pressure system located over the eastern side of the Tasman Sea and close to New Zealand is shown in Figure 9. During the afternoon, deep boundary layer depths can be seen over the Australian continent driven by daytime heating (Figure 9a), while they are substantially lower during the nighttime, as shown in Figure 9b. Deep boundary layer depths over the Southern Ocean were caused by intense cold advection, while the boundary layer reached moderate depths close to the cyclonic circulation center over the Tasman Sea.

[33] Vertical cross-sections over the eastern Tasman Sea and over the North Island of New Zealand along the line AB in Figure 9 are shown in Figure 10. Relatively high PM_{10} concentrations (up to ~400 μg m^{-3}) clearly illustrate the simulated long-range southeastward transport of Australian dust over the Tasman Sea. The peak dust values are predicted to be primarily located below around 3 km, demonstrating the low-level nature of dust transport. The low-level dust plume was predicted to be located over the west of Auckland at 0600 UTC on 24 September 2009 (Figure 10a), but shifted further east by 1200 UTC (Figure 10b). Given that ground-based measurements at Auckland indicate that PM_{10} concentrations started to increase at around 0900 UTC on 24 September and reached the maximum value of ~350 μg m^{-3} at around 1300 UTC (not shown), Figure 10 shows that the model adequately predicted the time of dust arrival over the region.

5.2. Dust Concentration Prior to and After the Arrival of the Cold Front

[34] The strong forcing imposed by the cold front is evident in the simulated vertical profiles of PM_{10} concentrations shown in Figure 11. It is clear that the cold front passed through the Elcombe region (29.97°S and 150.34°E), so that northwesterly winds were replaced by southwesterly winds (as shown by the isobars in Figure 11), causing the temperature to drop significantly. Before the air mass change, PM_{10} concentration is predicted to have increased

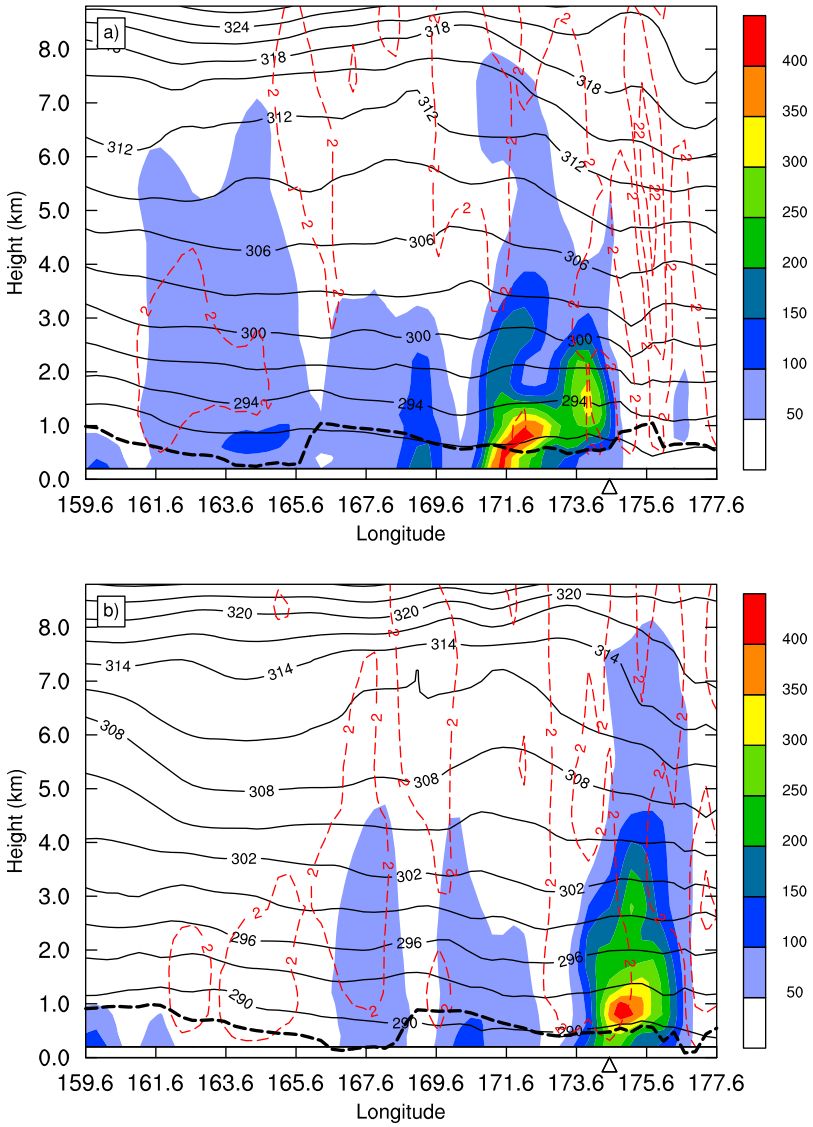

Figure 10. Similar to Figure 8, but cross-sections are along the line from A to B shown in Figure 9 at (a) 0600 UTC on 24 September and (b) 1200 UTC on 24 September 2009. The approximate location of Auckland is shown by the arrow on the X axis.

with height in the lower atmosphere (Figure 11c). This is due to the development of a very stable near-surface boundary layer accompanied by low particle concentrations primarily due to surface deposition. As a result, the maximum particle concentration occurred at around 1 km height in the residual layer. The passage of the cold front was predicted to produce a significant increase of surface PM_{10} concentrations reaching 5000 μg m^{-3}, around one order of magnitude greater than the values before the arrival of the cold front. Even with vigorous vertical mixing, the PM_{10} concentration declined with height as gravity tends to settle dust particles. Furthermore, boundary layer depth increased considerably from ~0.1 km in the pre-frontal to ~1.2 km in the post-frontal condition.

[35] Vertical distribution of mineral dust in the pre- and post-frontal conditions depends on the stratification of the atmosphere which can be evaluated by analyzing vertical profiles of potential temperature. These profiles derived from the WRF model for the Elcombe region are displayed in Figures 11c and 11d. The air mass change was predicted to cause a substantial decrease of surface potential temperature from 303 K to ~295 K and an increase of near-surface wind speeds (up to 4 m s^{-1}, not shown). Furthermore, before the arrival of the cold front, there is a nocturnal strongly stable near-surface layer, capped by a residual layer from the previous day, and a stable cap above that at around 2–3 km (Figure 11c). After the air mass change (Figure 11d), the near-surface layer is only weakly stable, before becoming well-mixed up to about 1 km, with a strong cap above that, indicating the contribution of the cold front to development of a well-mixed layer. Note that the inversion between ~1–1.8 km at 1800 UTC on 22 September may be related to the vertical structure of the cold front. As the cold front was tilted rearward with height, the near-surface layer

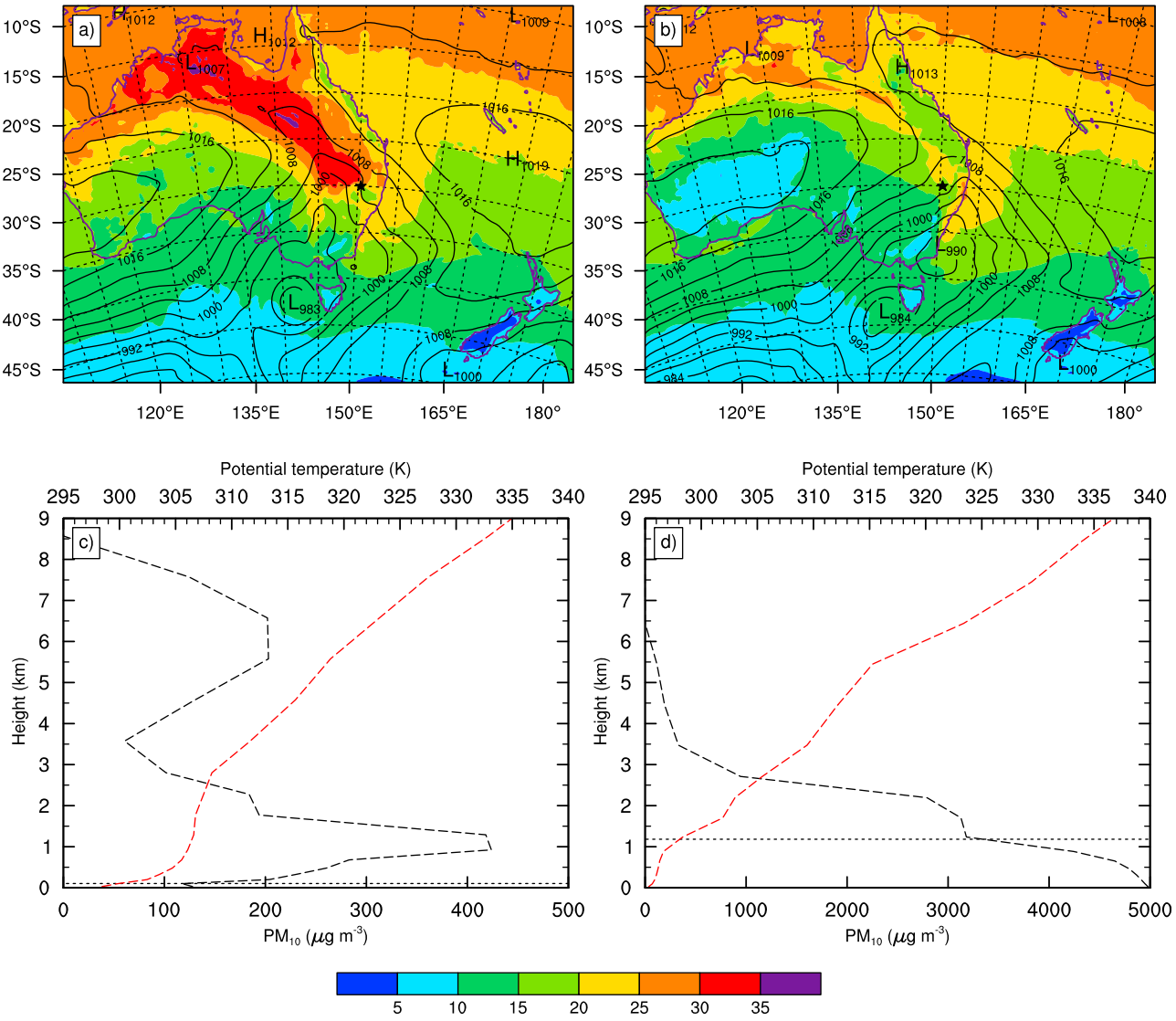

Figure 11. (a, b) Simulation of mean sea level pressure (contour interval of 4 hPa), 2-meter temperature (°C, as shown in scale) and (c, d) vertical profile of PM_{10} concentration (black dashed line, $\mu g\ m^{-3}$), PBL depth (black horizontal dotted line, km) and potential temperature (red dashed line, K) at Elcombe (29.97°S, 150.34°E, shown by the star), Australia at 1000 UTC (Figures 11a and 11c) and 1800 UTC (Figures 11b and 11d) on 22 September 2009. Note the different X axis scales in Figures 11c and 11d.

was in the post-frontal air mass, whereas air above ~1 km appears still to be in the pre-frontal air mass.

6. Vertical Structure of the Dust Plume Retrieved From CALIOP

[36] Vertical cross-sections from the CALIOP data set over the CALIPSO orbital paths along the lines AB in Figure 2 are given in Figures 12 and 13. Over central Australia at 1600 UTC on 22 September, a dust layer reached a height of approximately 2 km between ~20–25°S and 138.4–137.3°E (Figure 12a). Over western Australia, a well-mixed aerosol layer extended from the surface to around 0.5 km. There was also a small dust load over the north-western tropical region of Australia (~15°S, 122.3°E) which was lifted to around 4 km (although this is a little difficult to see in Figure 12b). During southeastward transport, the top of the dust plumes varied substantially, depending on the various atmospheric processes discussed in section 5.1, reaching up to 3 km over eastern Australia (Figure 13a) and the Tasman Sea (Figure 13b).

[37] Figure 14 shows vertical profiles of regionally averaged dust extinction coefficients at 532 nm over the CALIPSO orbital paths shown in Figure 2 (the latitude varies from 45–10°S). The extinction coefficient measures attenuation of light passing through the atmosphere due to scattering and absorption by dust aerosols. Over central Australia, the dust layer had a strong extinction coefficient peak at around 0.4 km and a second weaker peak at around 1.9 km (Figure 14a), while eastern Australia was associated with one major extinction coefficient peak near the surface reaching 0.6 km^{-1} and a second peak at 2 km height with a value of ~0.17 km^{-1} (Figure 14b). Over western Australia, two peaks close to the surface and around 1 km altitude were

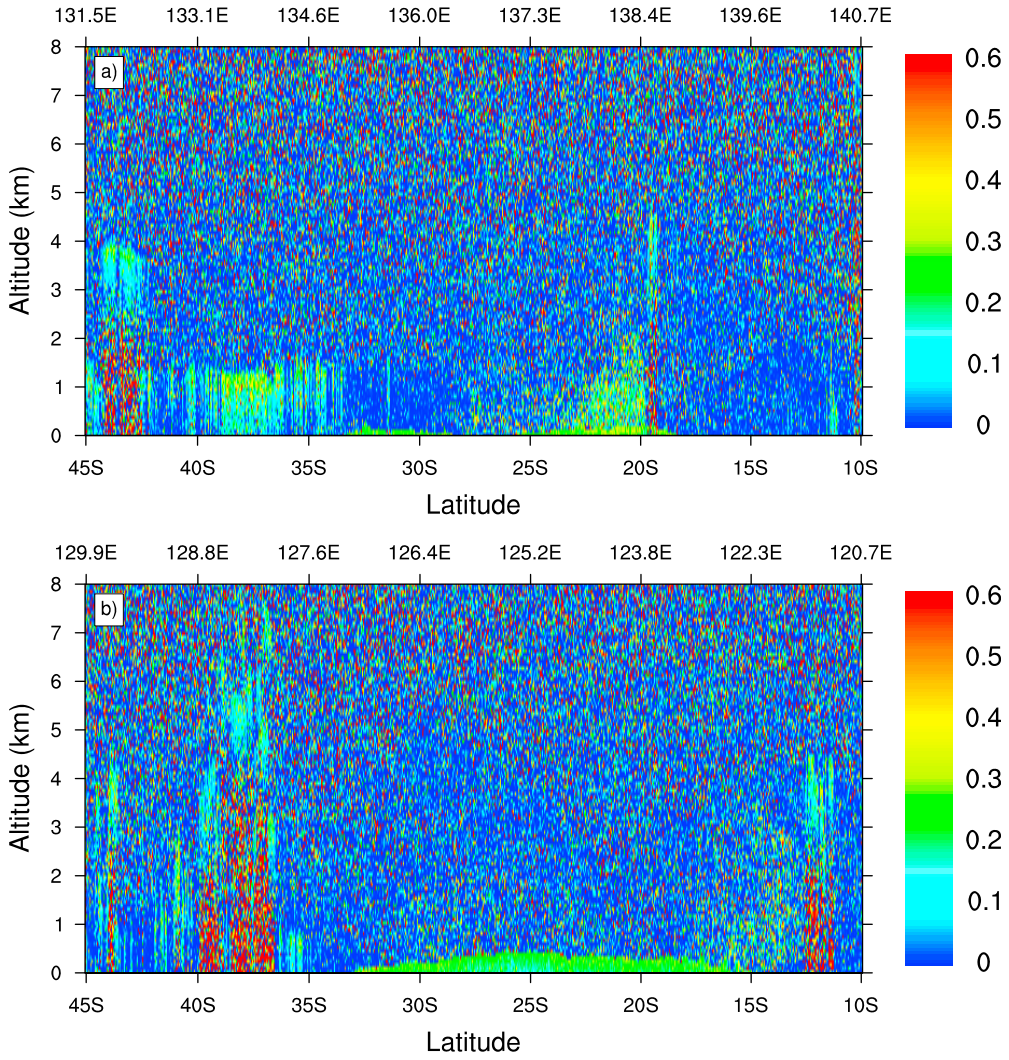

Figure 12. Depolarization ratio at 532 nm retrieved from the Level 1B CALIOP data sets during overpasses at around (a) 1600 UTC on 22 September and (b) 1637 UTC on 23 September 2009, corresponding to the CALIPSO orbit paths shown in Figures 2a and 2c, respectively. The top X axis shows the longitude values.

observed (Figure 14c), although the dust extinction coefficients over this area were substantially less (with a maximum value of 0.11 km^{-1}) than eastern Australia (with a maximum value of 0.6 km^{-1}). This indicates that only small quantities of dust were transported to western Australia, which is consistent with the eight-day MODIS data shown in Figure 5. High dust extinction coefficient values were observed over the Tasman Sea between 0.1 and 1.5 km above the ground, with three remarkable peaks at around 0.1, 0.6 and 1.1 km (Figure 14d). Although some dust particles were transported to the free atmosphere, primarily by strong ascending motion in the warm conveyor belt, the notable high dust extinction coefficients close to the surface over eastern Australia and the Tasman Sea suggest that dust was mainly transported within the atmospheric boundary layer. This is not surprising since Australian deserts are not surrounded by high mountains, so that lack of orographic forcing could contribute to the dominance of low-level dust transport from Australia. Figure 14d also reveals that there was an elevated dust layer between 4–4.6 km above ground which was separated from the lower dust layer, indicating a weak two-layer structure to the dust plume during its transport over the Tasman Sea.

7. Discussion and Conclusions

[38] The dust event during 22–23 September 2009 over Australia has been simulated using the WRF/Chem model with the MOSAIC aerosol module comprising 8 sectional bins less than 10 μm in diameter, the DUSTRAN module developed by *Shaw et al.* [2008], the YSU PBL scheme and meteorological conditions initialized using FNL reanalysis data from NCEP. The dust event was caused by the passage of a cold front associated with an intense extratropical cyclone over the Southern Ocean. The frontal system is particularly noteworthy, as it produced a major contribution to both the upward and horizontal transport of dust. The export of dust from Australia was significant since there was a severe drought and low rainfall for the three years prior to the dust event [*Zhao and Running*, 2010; *Leys et al.*, 2011],

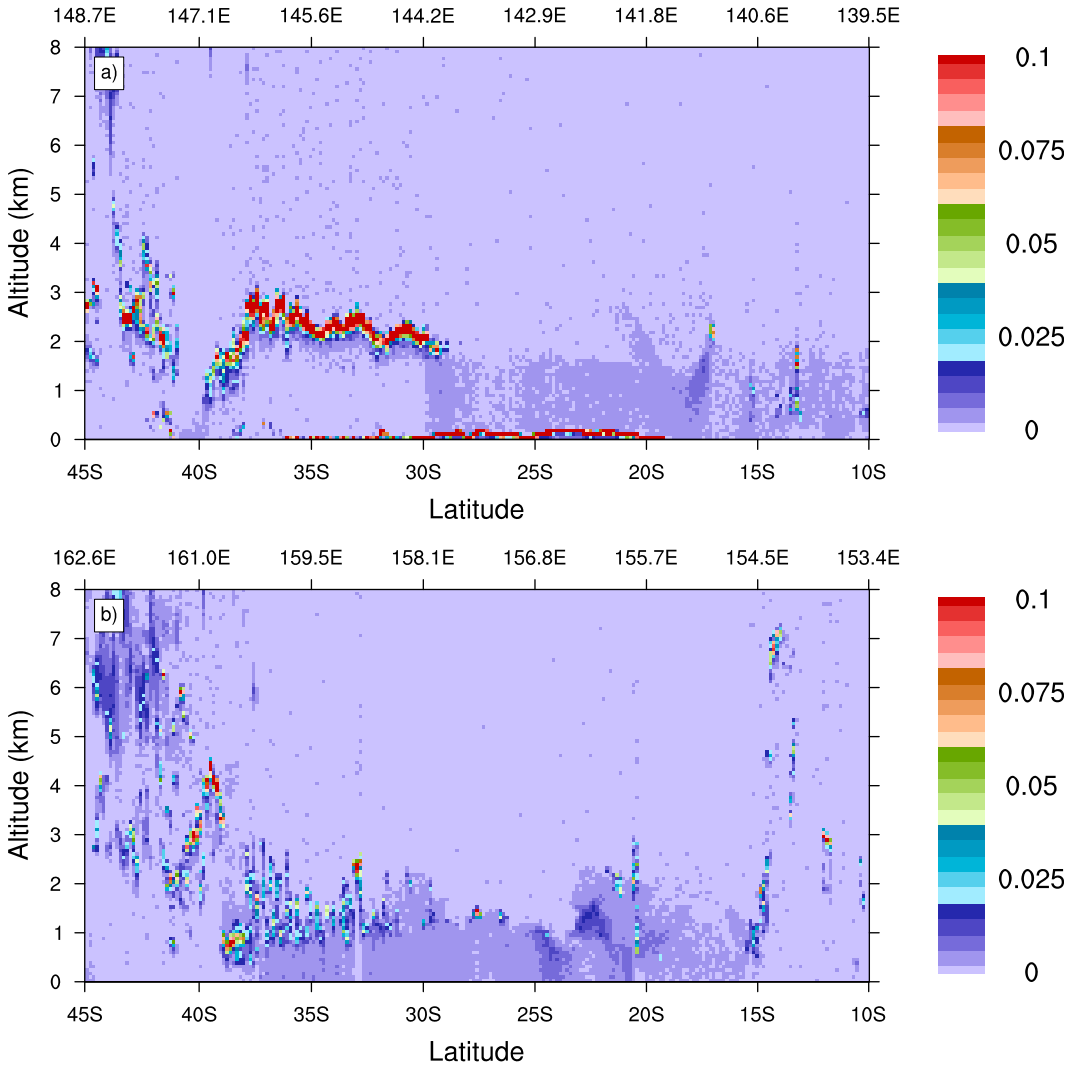

Figure 13. Total attenuated backscatter (km^{-1} sr^{-1}) at 532 nm retrieved from the Level 1B CALIOP data sets during overpasses at around (a) 0400 UTC on 23 September and (b) 0300 on 24 September 2009, corresponding to the CALIPSO orbit paths shown in Figures 2b and 2d, respectively. The top X axis shows the longitude values.

and dust particles were not removed by rainout during the course of transport.

[39] The simulated AOD was compared with satellite data and the model reproduced the dust pathway to the Tasman Sea and northern regions of Australia reasonably well. However, dust transport to northwestern Australia and finally to the Indian Ocean is overestimated by the model. Comparison of simulated results with ground-based measurements indicates good performance of the model over the study area except for New South Wales, where dust concentrations were significantly underestimated, probably due to underprediction of dust emission from grazing land and mining areas over New South Wales. Furthermore, before and after the peak dust concentrations when wind speeds were weaker, the model overestimated the observed values primarily because the threshold friction velocity was assumed to be constant in the simulation, while in reality it should be increased for fine particles as a result of the increase of inter-particle cohesion forces. Analysis of ground-based measurements indicates that southeastern (New South Wales) and eastern (e.g. Brisbane and Toowoomba in Queensland) Australia were downwind of major dust sources that supplied huge amounts of dust, over a short time period, while northeastern regions (e.g. Townsville Port) were downwind of a source region that supplied less intense dust, but for a longer period [*Leys et al.*, 2011].

[40] Simulation of dust transport routes and MODIS data (Figure 4) highlight two main transport pathways of Australian dust-laden air during such events. First, there is a pathway to the Tasman Sea off the southeast coast of Australia as a result of pre-frontal northwesterly winds and eastward moving frontal system, and to northern Australia and to the Coral Sea, Gulf of Carpentaria, Arafura Sea and Timor Sea by post-frontal southwesterly winds and associated anticyclonic circulation. The latitudinal transport of dust to northern Australia by the high-pressure circulation is similar to the Atlantic Ocean where the Azores-Bermuda anticyclonic circulation transports aerosol-laden air from the

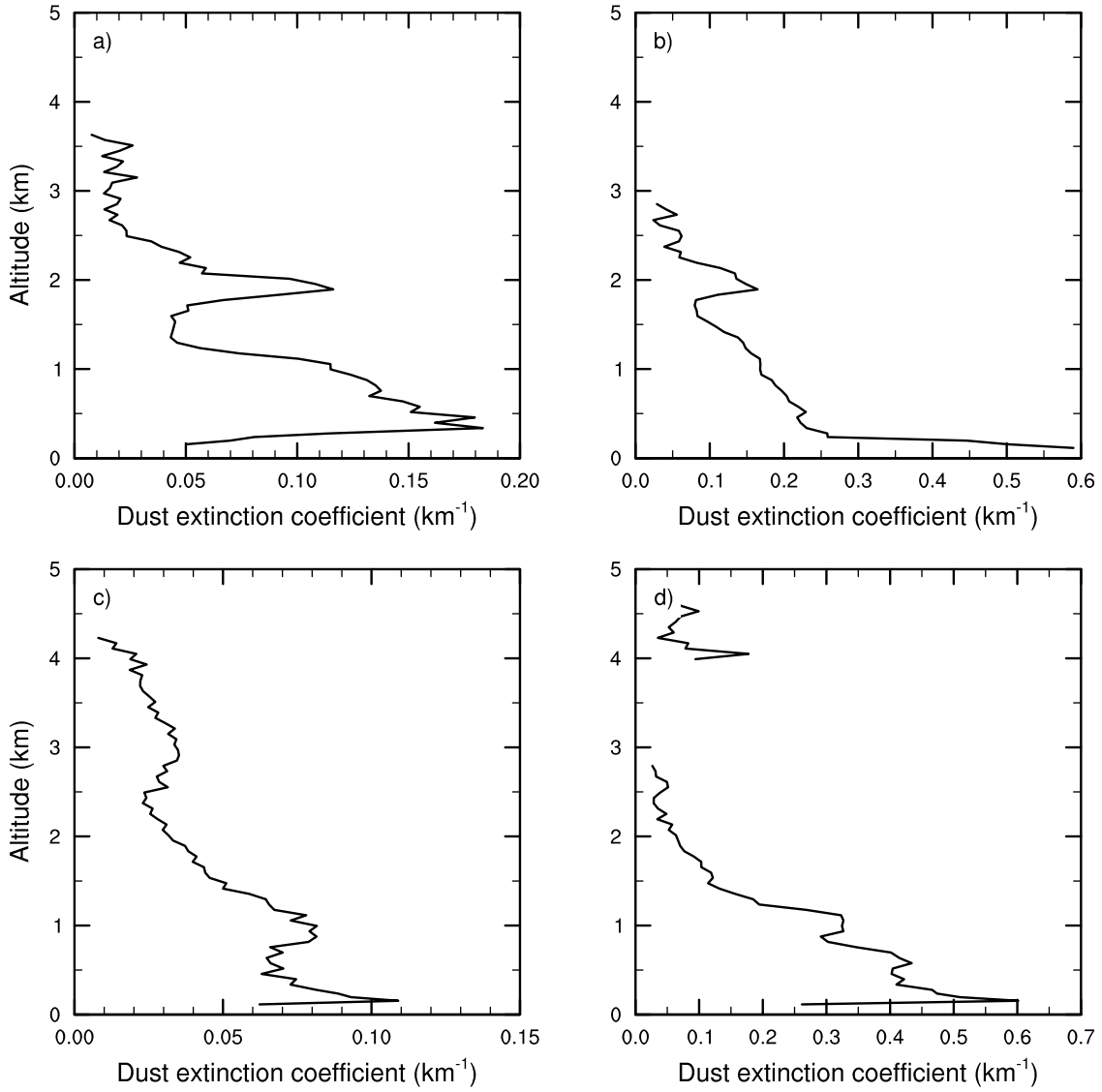

Figure 14. Vertical profiles of regionally averaged (corresponding to the CALIPSO orbit paths shown in Figure 2) dust aerosol extinction coefficients (km^{-1}) derived from CALIOP data set at around (a) 1600 UTC on 22 September, (b) 0400 UTC on 23 September, (c) 1637 UTC on 23 September, and (d) 0300 UTC on 24 September 2009. Note the different X axis scales in all panels.

tropical Atlantic (originating from North African dust episodes and biomass burning) to subtropical regions [*Goudie and Middleton*, 2001]. CALIOP observations indicate that transport of dust southeastward to the Tasman Sea was significantly greater than to other regions. This is expected because of the prevailing westerlies through the midlatitude troposphere combined with eastward moving frontal systems, as well as pre-frontal northwesterly winds that carry dust plumes to the Tasman Sea. Model results also revealed the potential for some limited transport of dust to the Indian Ocean caused by the anticlockwise circulation of the high-pressure system located over western and central Australia after the passage of the cold front, as well as the southeasterly trade winds over northern tropical Australia, but such transport is not supported by the MODIS data and appears to be overestimated. Previous research only identified two exit paths of Australian dust: southeastward to the Tasman Sea associated with easterly moving frontal systems and northwestward to the Indian Ocean due to southeasterly trade winds in the north tropical regions [*Knight et al.*, 1995]. However, our results show that quite significant amounts of dust may be transported to northern Australia (with eight-day AOD values more than 0.6 as shown in Figure 5), extending from the Coral Sea northeast of Australia to the Timor Sea to the northwest. This means that in addition to New Zealand to the southeast of Australia, countries to the north can also be affected by severe Australian dust storms.

[41] Model simulation results indicate that there was a significant variation in boundary layer structure during the passage of cold frontal systems across Australia. Boundary layer depth was deeper behind the cold front due to strong cold advection over relatively warm surfaces. This region was also associated with the maximum PM_{10} concentrations as a result of strong near-surface wind speeds. This suggests

that dust was mainly being picked up from the surface by post-frontal winds, consistent with the results of *Leys et al.* [2011]. Dust particles were then mixed through the depth of the boundary layer behind the cold front, due to the substantial turbulent mixing in the well-mixed boundary layer. Over the area dominated by anticyclonic circulation, particle concentrations were low and less elevated. Large-scale descending motion trapped the particles in lower layers of the atmosphere, and subsequent horizontal transport toward low-pressure regions occurred by divergent winds around the fringes of the anticyclone. In the warm sector ahead of the cold front, boundary layer depth was relatively shallow due to warm advection over cold surfaces. However, warm advection contributed to strong ascending motions in the conveyor belt along the frontal zone, which appears to contribute to transport of some dust to the free atmosphere. Indeed, simulation results suggest that the maximum height that the dust plume could reach (~8 km) was ahead of the cold front, suggesting that the warm conveyor belt is the most important mechanism for transporting particles from the boundary layer to the free atmosphere.

[42] As we often observe stronger wind speeds in the free atmosphere than the boundary layer, dust particles within the free atmosphere tend to be transported longer distances and affect downwind regions further away from the source of dust. Furthermore, there is no dry deposition in the free atmosphere, and hence, dust particles have longer atmospheric lifetimes, which in turn enhance their climate forcing. Consequently, transport of particles from the boundary layer to the free atmosphere associated with the ascending motion along the leading edge of the cold front is a key process linking local dust sources to regional and global distribution of dust aerosols.

[43] Analysis of CALIOP data indicates that dust originating from Australia can extend to more than 4 km above the ground (Figure 14). CALIOP observations detected a layer with high dust extinction coefficient values from near the surface to around 3 km over eastern Australia and the Tasman Sea (with a maximum value of 0.6 km^{-1} close to the surface). Another dust layer with a smaller dust extinction coefficient (with a maximum value of 0.15 km^{-1}) was observed at around 4–4.6 km over the Tasman Sea, which was unconnected with the near-surface dust layer. These results suggest that Australian dust can be transported toward New Zealand and beyond within both the lower and mid-troposphere. This two-layer dust transport is similar to the structures identified over eastern China and the western Pacific Ocean, associated with contributions from two major dust sources: the Gobi and Taklamakan deserts [*Huang et al.*, 2008].

[44] Although model simulation results indicate that some of the dust can reach as high as ~8 km ahead of the cold front, these dust aerosols were not detected by the CALIOP data, except in Figure 14d where the previously mentioned elevated dust layer was observed. This might be caused by the fact that the orbit paths of the selected CALIOP data are not coincide with the location of the warm conveyor belt. In addition, simulation results indicate that significant amounts of Australian dust remained in the lower atmosphere, primarily within the boundary layer, and only relatively small quantities transported to an altitude of more than 4 km (Figures 8 and 10). Consequently, model simulations indicate that in this event most of the dust was transported within the lower atmosphere. Low-level transport of Australian dust was partly caused by the lack of significant orography, so that dust plumes were less affected by upward motion induced by orographic forcing. This is in contrast to the Taklamakan desert where low-level dust transport is trapped by surrounding high mountains, so that orographic forcing advects dust vertically to the free atmosphere [*Uno et al.*, 2009], and hence a concentrated dust layer was observed at around 3 km [*Huang et al.*, 2008]. However, the situation in Australia is similar to boundary layer dust transport from the Gobi desert of southern Mongolia and northern China [*Uno et al.*, 2009]. Also, with vigorous mixing occurring behind the cold front, the high near-surface PM_{10} concentrations shown in Figures 8 and 10 could be caused by the fact that dust particles are typically in the coarse particle size range and gravitational settling prevented significant amounts of them being transported to higher levels.

[45] Since dust plumes were mostly transported in the lower atmosphere over the Tasman Sea, in contrast to the Saharan Air Layer (SAL) over the Atlantic Ocean [*Liu et al.*, 2008], it is expected that dust aerosols would become mixed with other aerosols types, such as sea salt, leading to changes in chemical composition and size of the aerosols, which in turn affects their optical properties. The dominance of dust transport within the boundary layer also suggests that Australian dust aerosols only slightly perturb the surface temperature, because heating of the dust layer associated with absorption of radiation by dust aerosols offsets the surface cooling (due to reflection of shortwave radiation by dust) through exchange of heat between the dust layer and the surface by turbulent mixing within the atmospheric boundary layer [*Miller and Tegen*, 1998]. This is in contrast to North African [*Liu et al.*, 2008] and Asian (Taklamakan) [*Huang et al.*, 2008] dust source regions where layers have been identified at much greater height above ground, which can have a larger surface cooling effect. Furthermore, since annual dust emission from Australia is significantly lower than North Africa and Asia [*Shao et al.*, 2007; *Rotstayn et al.*, 2009], this further supports the idea that Australian dust has a lesser impact on regional and global climate compared to the other main dust source areas in the Northern Hemisphere.

[46] Model simulations show that dust is deposited largely over the Tasman Sea, where dry removal is the dominant process because dust was mainly transported within the boundary layer and lower troposphere, and therefore subject to deposition by gravitational settling and turbulent eddies. The substantial dry deposition of Australian dust is evident by comparing the maximum PM_{10} concentrations over eastern Australia (~2600 $\mu g\ m^{-3}$) with those over the central (~1400 $\mu g\ m^{-3}$) and eastern (~400 $\mu g\ m^{-3}$) Tasman Sea. As Australian dust is high in iron content [*Rotstayn et al.*, 2009], the substantial dry deposition over the Tasman Sea can lead to phytoplankton blooms, and therefore can increase atmospheric CO_2 uptake.

[47] The conclusions from this study are only based on a single dust event during 22–23 September 2009 and do not necessarily imply that dust transport paths and vertical distribution are similar for other dust episodes. Long-term

observation and model simulation and their analysis are necessary to determine the typical vertical distribution and transport pathways of Australian dust.

[48] **Acknowledgment.** We would like to thank three anonymous reviewers for their detailed and helpful comments.

References

Binkowski, F., and U. Shankar (1995), The Regional Particulate Matter Model: 1. Model description and preliminary results, *J. Geophys. Res.*, *100*(D12), 26,191–26,209, doi:10.1029/95JD02093.

Bluestein, H. B. (1992), *Synoptic-Dynamic Meteorology in Midlatitudes*, Oxford Univ. Press, New York.

Chapman, E., W. Gustafson, R. Easter, J. Barnard, S. Ghan, M. Pekour, and J. Fast (2009), Coupling aerosol-cloud-radiative processes in the WRF-Chem model: Investigating the radiative impact of elevated point sources., *Atmos. Chem. Phys.*, *9*(3), 945–964.

Chen, F., and J. Dudhia (2001), Coupling an advanced land surface-hydrology model with the Penn State-NCAR MM5 modeling system. Part I: Model implementation and sensitivity, *Mon. Weather Rev.*, *129*(4), 569–585.

Chung, C., and G. Zhang (2004), Impact of absorbing aerosol on precipitation: Dynamic aspects in association with convective available potential energy and convective parameterization closure and dependence on aerosol heating profile, *J. Geophys. Res.*, *109*, D22103, doi:10.1029/2004JD004726.

Eckhardt, S., A. Stohl, H. Wernli, P. James, C. Forster, and N. Spichtinger (2004), A 15-year climatology of warm conveyor belts, *J. Clim.*, *17*(1), 218–237.

Ek, M. B., K. E. Mitchell, Y. Lin, E. Rogers, P. Grunmann, V. Koren, G. Gayno, and J. D. Tarpley (2003), Implementation of Noah land surface model advances in the National Centers for Environmental Prediction operational mesoscale Eta model, *J. Geophys. Res.*, *108*(D22), 8851, doi:10.1029/2002JD003296.

Fecan, F., B. Marticorena, and G. Bergametti (1998), Parametrization of the increase of the aeolian erosion threshold wind friction velocity due to soil moisture for arid and semi-arid areas, *Ann. Geophys.*, *17*(1), 149–157.

Goudie, A. S., and N. J. Middleton (2001), Saharan dust storms: Nature and consequences, *Earth Sci. Rev.*, *56*(1), 179–204.

Goudie, A. S., and N. Middleton (2006), *Desert Dust in the Global System*, Springer, New York.

Grell, G. (1993), Prognostic evaluation of assumptions used by cumulus parameterizations, *Mon. Weather Rev.*, *121*(3), 764–787.

Hong, S. Y. (2010), A new stable boundary-layer mixing scheme and its impact on the simulated East Asian summer monsoon, *Q. J. R. Meteorol. Soc.*, *136*(651), 1481–1496.

Hong, S. Y., Y. Noh, and J. Dudhia (2006), A new vertical diffusion package with an explicit treatment of entrainment processes, *Mon. Weather Rev.*, *134*(9), 2318–2341.

Huang, J., B. Lin, P. Minnis, T. Wang, X. Wang, Y. Hu, Y. Yi, and J. Ayres (2006), Satellite-based assessment of possible dust aerosols semi-direct effect on cloud water path over East Asia, *Geophys. Res. Lett.*, *33*, L19802, doi:10.1029/2006GL026561.

Huang, J., P. Minnis, B. Chen, Z. Huang, Z. Liu, Q. Zhao, Y. Yi, and J. K. Ayers (2008), Long-range transport and vertical structure of Asian dust from CALIPSO and surface measurements during PACDEX, *J. Geophys. Res.*, *113*, D23212, doi:10.1029/2008JD010620.

Huang, J., Q. Fu, J. Su, Q. Tang, P. Minnis, Y. Hu, Y. Yi, and Q. Zhao (2009), Taklimakan dust aerosol radiative heating derived from CALIPSO observations using the Fu-Liou radiation model with CERES constraints, *Atmos. Chem. Phys.*, *9*(12), 4011–4021.

Knight, A., G. McTainsh, and R. Simpson (1995), Sediment loads in an Australian dust storm: Implications for present and past dust processes, *Catena*, *24*(3), 195–213.

Kowol-Santen, J., M. Beekmann, S. Schmitgen, and K. Dewey (2001), Tracer analysis of transport from the boundary layer to the free troposphere, *Geophys. Res. Lett.*, *28*(15), 2907–2910, doi:10.1029/2001GL012908.

Leys, J. F., S. K. Heidenreich, C. L. Strong, G. H. McTainsh, and S. Quigley (2011), PM_{10} concentrations and mass transport during "Red Dawn"–Sydney 23 September 2009, *Aeolian Res.*, *3*(3), 327–342.

Lin, Y. L., R. D. Farley, and H. D. Orville (1983), Bulk parameterization of the snow field in a cloud model, *J. Clim. Appl. Meteorol.*, *22*(6), 1065–1092.

Liu, Z., et al. (2008), CALIPSO lidar observations of the optical properties of Saharan dust: A case study of long-range transport, *J. Geophys. Res.*, *113*, D07207, doi:10.1029/2007JD008878.

McGowan, H., G. McTainsh, P. Zawar-Reza, and A. Sturman (2000), Identifying regional dust transport pathways: Application of kinematic trajectory modelling to a trans-Tasman case, *Earth Surf. Processes Landforms*, *25*(6), 633–647.

McGowan, H. A., B. Kamber, G. H. McTainsh, and S. K. Marx (2005), High resolution provenancing of long travelled dust deposited on the Southern Alps, New Zealand, *Geomorphology*, *69*(1–4), 208–221.

McTainsh, G., Y. Chan, H. McGowan, J. Leys, and K. Tews (2005), The 23rd October 2002 dust storm in eastern Australia: Characteristics and meteorological conditions, *Atmos. Environ.*, *39*(7), 1227–1236.

Miller, R., and I. Tegen (1998), Climate response to soil dust aerosols, *J. Clim.*, *11*(12), 3247–3267.

Obukhov, A. M. (1971), Turbulence in an atmosphere with a non-uniform temperature, *Boundary Layer Meteorol.*, *2*(1), 7–29.

Remer, L., et al. (2005), The MODIS aerosol algorithm, products, and validation, *J. Atmos. Sci.*, *62*(4), 947–973.

Rotstayn, L., M. Keywood, B. Forgan, A. Gabric, I. Galbally, J. Gras, A. Luhar, G. McTainsh, R. Mitchell, and S. Young (2009), Possible impacts of anthropogenic and natural aerosols on Australian climate: A review, *Int. J. Climatol.*, *29*(4), 461–479.

Shao, Y. (2008), *Physics and Modelling of Wind Erosion*, Springer Sci., New York.

Shao, Y., J. F. Leys, G. H. McTainsh, and K. Tews (2007), Numerical simulation of the October 2002 dust event in Australia, *J. Geophys. Res.*, *112*, D08207, doi:10.1029/2006JD007767.

Shaw, W., K. Allwine, B. Fritz, F. Rutz, J. Rishel, and E. Chapman (2008), An evaluation of the wind erosion module in DUSTRAN, *Atmos. Environ.*, *42*(8), 1907–1921.

Sinclair, V. A., S. L. Gray, and S. E. Belcher (2008), Boundary-layer ventilation by baroclinic life cycles, *Q. J. R. Meteorol. Soc.*, *134*(635), 1409–1424.

Sinclair, V. A., S. E. Belcher, and S. L. Gray (2010), Synoptic controls on boundary-layer characteristics, *Boundary Layer Meteorol.*, *134*(3), 387–409.

Trewin, B., and H. Vermont (2010), Changes in the frequency of record temperatures in Australia, 1957–2009, *Aust. Meteorol. Oceanogr. J.*, *60*(2), 113–119.

Uno, I., K. Eguchi, K. Yumimoto, T. Takemura, A. Shimizu, M. Uematsu, Z. Liu, Z. Wang, Y. Hara, and N. Sugimoto (2009), Asian dust transported one full circuit around the globe, *Nat. Geosci.*, *2*(8), 557–560.

Wild, O., X. Zhu, and M. J. Prather (2000), Fast-J: Accurate simulation of in- and below-cloud photolysis in tropospheric chemical models, *J. Atmos. Chem.*, *37*(3), 245–282.

Winker, D. M., W. H. Hunt, and M. J. McGill (2007), Initial performance assessment of CALIOP, *Geophys. Res. Lett.*, *34*, L19803, doi:10.1029/2007GL030135.

Zaveri, R. A., R. C. Easter, J. D. Fast, and L. K. Peters (2008), Model for simulating aerosol interactions and chemistry (MOSAIC), *J. Geophys. Res.*, *113*, D13204, doi:10.1029/2007JD008782.

Zhao, M., and S. W. Running (2010), Drought-induced reduction in global terrestrial net primary production from 2000 through 2009, *Science*, *329*(5994), 940–943.